

Global strain-induced scalar potential in graphene devices

Lujun Wang ^{1,2}✉, Andreas Baumgartner ^{1,2}, Péter Makk^{1,3}, Simon Zihlmann ¹, Blesson Sam Varghese¹, David I. Indolese¹, Kenji Watanabe ⁴, Takashi Taniguchi ⁵ & Christian Schänenberger ^{1,2}

By mechanically distorting a crystal lattice it is possible to engineer the electronic and optical properties of a material. In graphene, one of the major effects of such a distortion is an energy shift of the Dirac point, often described as a scalar potential. We demonstrate how such a scalar potential can be generated systematically over an entire electronic device and how the resulting changes in the graphene work function can be detected in transport experiments. Combined with Raman spectroscopy, we obtain a characteristic scalar potential consistent with recent theoretical estimates. This direct evidence for a scalar potential on a macroscopic scale due to deterministically generated strain in graphene paves the way for engineering the optical and electronic properties of graphene and similar materials by using external strain.

¹Department of Physics, University of Basel, Basel, Switzerland. ²Swiss Nanoscience Institute, University of Basel, Basel, Switzerland. ³Department of Physics, Budapest University of Technology and Economics and Nanoelectronics Momentum Research Group of the Hungarian Academy of Sciences, Budapest, Hungary. ⁴Research Center for Functional Materials, National Institute for Material Science, Tsukuba, Japan. ⁵International Center for Materials Nanoarchitectonics, National Institute for Materials Science, Tsukuba, Japan. ✉email: lujun.wang@unibas.ch

Graphene is a model system on which a large variety of new and prominent physical phenomena have been discovered^{1–4}. A particularly promising topic is the control of its electronic properties by external strain, which has been extensively studied theoretically. The predicted strain effects in the low-energy band structure of graphene can be summarized as changes in the magnitude and isotropy of the Fermi velocity and thus in the density of states^{5–8}, shifts in the energy of the Dirac point, which is typically incorporated as a scalar potential^{6,8,9}, and changes in the position of the Dirac cone in the two-dimensional Brillouin zone, often described by a pseudo-vector potential acting on the valley degree of freedom^{9–14}. Previous experiments explored some of these strain effects on a local scale using scanning tunneling microscopy^{15–23}, Kelvin probe force microscopy^{24,25}, or angle-resolved photoemission spectroscopy²⁶. However, studying strain effects in transport measurements and on a global scale is still challenging due to the lack of in situ strain tunability^{21,27,28} or ambiguities resulting from simultaneous changes in the gate capacitance^{29–31}.

Here, we demonstrate the formation of a scalar potential generated by systematically tuning the strain in a micrometer sized graphene electronic device and investigate its effects on two fundamental electron transport phenomena, quasi-ballistic transport and the quantum Hall effect (QHE). We find that all investigated transport characteristics are shifted systematically in gate voltage, qualitatively and quantitatively consistent with the expectations for the scalar potential generated by the applied strain, where the strain values are confirmed by separate Raman spectroscopy experiments.

Results

Device and strain generation. The work function (WF) of a material, i.e., the energy required to remove an electron from the material, is defined as the difference between the vacuum level E_{vac} and the Fermi level E_F of the material³². For undoped graphene, E_F coincides with the Dirac point energy E_D ¹, therefore the WF of undoped graphene is $W_G^0 = E_{\text{vac}} - E_D$. A strain-induced scalar potential shifts E_D , which therefore leads to a change in W_G^0 . With increasing tensile strain, the scalar potential shifts E_D to lower values, resulting in an increase in W_G^0 ^{6,8}, as illustrated in Fig. 1a. Quantitatively, strain shifts E_D to $\tilde{E}_D = E_D + S$, where S is the scalar potential, and can be written as^{6,8,9}:

$$S(x, y) = -s_0 \cdot (\varepsilon_{xx} + \varepsilon_{yy}), \quad (1)$$

with ε_{xx} and ε_{yy} the diagonal components of the strain tensor, and s_0 a constant defined for small strain values. The value of s_0 is not well established and theoretical values are reported in the range between 2.5 eV and 4.1 eV^{6,8,9}.

How we generate strain in our experiments in an on-chip fully encapsulated graphene device is illustrated in Fig. 1b: in a three-point bending setup a 24 mm × 9.5 mm × 0.3 mm flexible substrate with the devices fabricated in the center is bent by pushing a central wedge against two fixed counter supports by a displacement of Δz ³¹. The schematics of the device configuration are shown in Fig. 1c. The edge contacts to graphene act as clamps for the strain generation and at the same time as electrical contacts for transport experiments³¹. A metallic global bottom gate is used to tune the charge carrier density in the device. The on-chip hBN encapsulation ensures that the geometrical capacitance between the gate and the graphene is not changed in the straining process. Here, we investigate strain effects on devices with a rectangular geometry, which results in an essentially homogeneous uniaxial strain field. Details of the device fabrication and the strain field pattern are discussed in a previous study³¹.

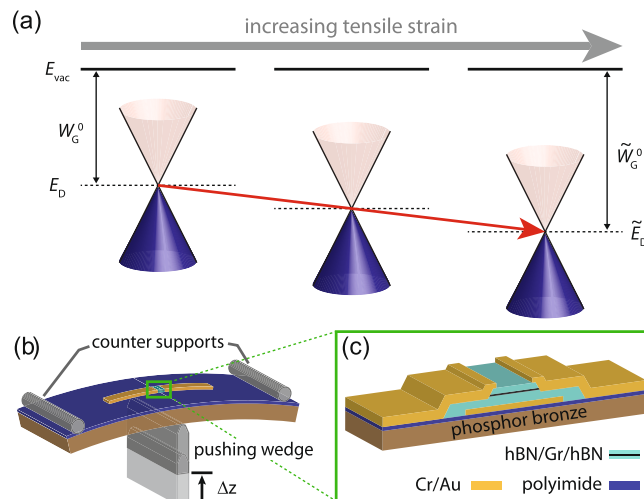


Fig. 1 Schematic representation of inducing scalar potential by strain.

a Illustration of the strain induced shift of the Dirac point. The vacuum level is labeled with E_{vac} , and the Dirac point and the work function of unstrained (strained) graphene with E_D (\tilde{E}_D) and W_G^0 (\tilde{W}_G^0), respectively. **b** Schematics of the three-point bending setup and **c** the encapsulated graphene device. The displacement Δz of the pushing wedge controls the bending of the substrate and thus the induced strain in the graphene.

In our devices, the grounded graphene sheet and the metallic gate essentially form a plate capacitor. The detailed diagram of energy level alignment and its modification by strain is given in Supplementary Note 1. The strain-induced scalar potential shifts the Dirac point, resulting in a systematic change in the charge carrier density of the device at a given gate voltage, which we detect in transport experiments.

Measurements at zero magnetic field. To investigate the strain effect, we perform transport experiments at liquid helium temperature ($T \approx 4.2$ K) using standard low-frequency lock-in techniques. The two-terminal differential conductance $G = dI/dV$ of a square device is measured as a function of V_g for different bendings Δz of the substrate. An overview measurement is plotted in Fig. 2a, on the scale of which no significant strain effects can be observed. The charge neutrality point (CNP) occurs at a positive gate voltage. From a linear fit near the CNP we find a field-effect charge carrier mobility of $\sim 130,000 \text{ cm}^2 \text{ V}^{-1} \text{ S}^{-1}$, independent of Δz , suggesting a high device quality and that random strain fluctuations are probably not dominating scattering processes here³³. The additional conductance minimum at $V_g \approx -1.2$ V may originate from a large contact doping due to the overlap of the electrodes with the graphene region near the edge contacts³⁴, or from a super-superlattice effect in encapsulated graphene when both the top and the bottom hBN layers are aligned to the graphene lattice³⁵.

The zoom-in to the CNP plotted in Fig. 2b shows very regular oscillations in conductance, which we tentatively attribute to Fabry-Pérot resonances in the regions near the electrical contacts with different doping compared to the graphene bulk^{36–39} (see Supplementary Note 2 for a detailed discussion). With increasing Δz and therefore increasing tensile strain, these conductance oscillations are shifted systematically to lower gate voltages. This effect is fully reversible with decreasing Δz , which is demonstrated in Supplementary Note 3. The strain-induced shift is best seen by following the CNP: in the inset of Fig. 2b we plot the gate voltage of minimum conductance, V_{CNP} as a function of Δz , which shows a linear decrease with increasing Δz , consistent with the picture described in the Supplementary Note 1. To demonstrate that the

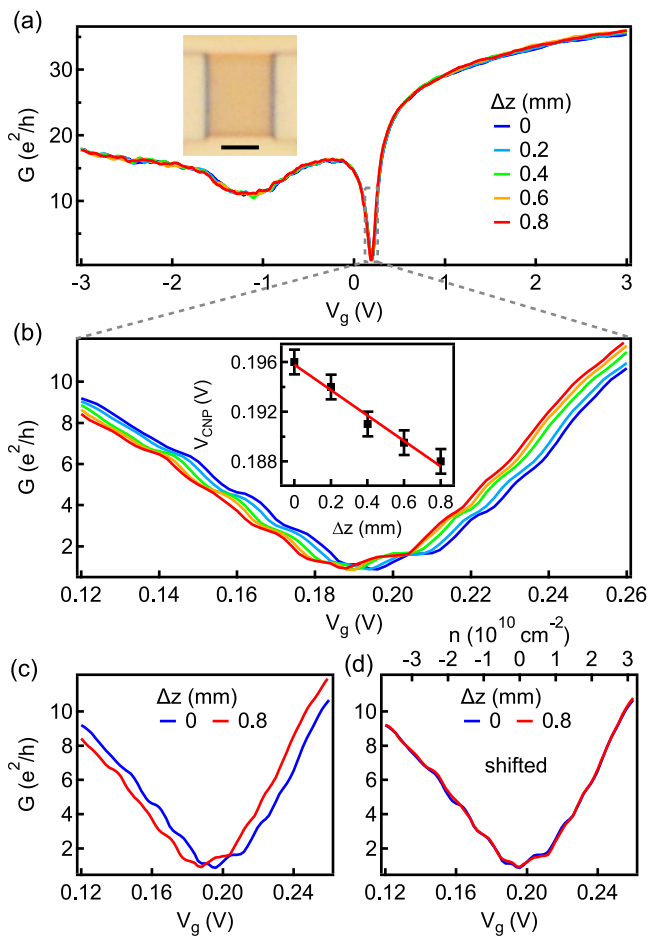


Fig. 2 Low-temperature transport measurements. **a** Two-terminal differential conductance G as a function of the gate voltage V_g for different displacement Δz . Inset: optical image of the measured device, scale bar: $2 \mu\text{m}$. **b** Zoom-in on the charge neutrality point (CNP). Inset: position of the CNP (V_{CNP}) as a function of Δz . V_{CNP} is extracted as the gate voltage of minimum conductance. The error bars are estimated from half of the measurement step size in V_g . Red line is a linear fit with a slope of about -10 mV per mm . **c** Zoom-in on the CNP for $\Delta z = 0$ and $\Delta z = 0.8 \text{ mm}$. **d** Same data as in (c) with the $\Delta z = 0.8 \text{ mm}$ curve (red) shifted to the right by $+8 \text{ mV}$ in V_g . The corresponding carrier density is shown on the top axis.

complete conductance curves are shifted with strain, we plot in Fig. 2c the two curves with the lowest ($\Delta z = 0$) and the highest ($\Delta z = 0.8 \text{ mm}$) strain values, and in Fig. 2d the same data, but with the $\Delta z = 0.8 \text{ mm}$ curve (red) shifted by $+8 \text{ mV}$ in V_g . We find that all conductance curves merge to the same curve as at $\Delta z = 0$ (blue) when shifted by a constant gate voltage offset. This shift we attribute to a strain-induced scalar potential in the graphene sheet.

Measurements in the quantum Hall regime. To demonstrate that our finding is a general phenomenon, independent of the device and the origin of the transport characteristics, we have investigated more than 5 devices, all of which exhibit shifts in the discussed direction and of similar magnitude. However, the pure shift of the complete conductance curve we find only in the device with a high mobility ($>100,000 \text{ cm}^2 \text{ V}^{-1} \text{ s}^{-1}$), while in samples of lower mobility, the effect of the global scalar potential is superimposed on other effects (see the Supplementary Note 4–6 for additional examples, one of which with opposite offset doping). Here, we now focus on the impact of homogeneous uniaxial

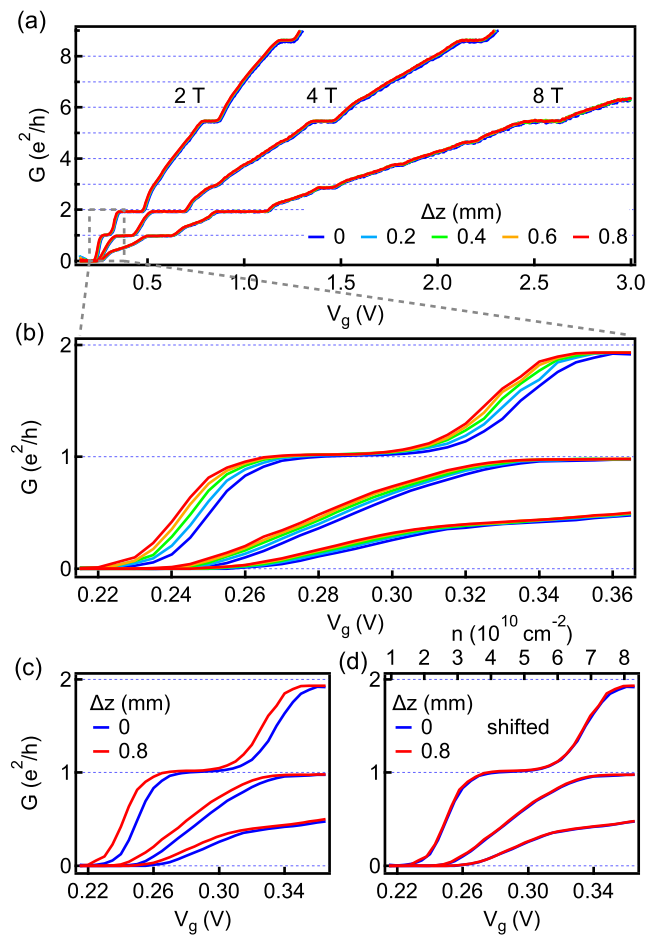


Fig. 3 Measurements in the quantum Hall regime. **a** Two-terminal differential conductance as a function of gate voltage V_g at three different quantizing magnetic fields for different displacement Δz . **b** Zoom-in to a small region in (a), showing the shift of the curves in V_g with increasing Δz . **c** Same as in (b) for $\Delta z = 0$ and $\Delta z = 0.8 \text{ mm}$. **d** Same as in (c) with the $\Delta z = 0.8 \text{ mm}$ curve (red) shifted to the right by 8 mV in V_g . The corresponding carrier density is shown on the top axis.

strain on the QHE in the same device, and perform a similar analysis as for the zero field measurements. Figure 3(a) shows the two-terminal differential conductance as a function of the gate voltage for three different quantizing magnetic fields, B , and for different Δz values. Typical quantum Hall plateaus of graphene can be observed on the electron side, with small deviations of the plateau conductances from the quantized values $2, 6, 10 e^2/h$ due to the contact resistance. The plateaus at the filling factors $\nu = 0$ and $\nu = 1$ are well developed already at $B = 2 \text{ T}$, and more broken symmetry states and fractional quantum Hall states can be observed at $B = 8 \text{ T}$ ^{40–42}, again highlighting the very good device quality. In contrast, the plateaus on the hole side are not well developed (see Supplementary Note 4) presumably due to a p-n junction forming near the contacts^{43,44}. Comparing the measurements for different Δz on this scale shows no clear strain effects. However, in the data near the CNP shown in Fig. 3b, we again find a systematic shift in V_g with increasing Δz . The clear offset between the $\Delta z = 0.8 \text{ mm}$ curve (red) and the $\Delta z = 0$ curve (blue) is shown in Fig. 3c. Shifting the red curve by $+8 \text{ mV}$, as shown in Fig. 3d, the two curves are virtually identical, in the same manner and with the same shift as discussed for Fig. 2 with the device at zero magnetic field. Since the QHE is quite a different transport regime than quasi-ballistic transport, the

observed effect is very general and we attribute it to a strain-induced scalar potential.

Discussion

We now extract the scalar potential from the transport experiments by evaluating the shift between the minimum ($\Delta z = 0$) and maximum strain ($\Delta z = 0.8$ mm). We assume that a specific conductance feature, for example, the CNP, or a QHE transition, occurs at a characteristic carrier density. Here we use the CNP as an example for extracting the scalar potential. Figure 4 shows the energy level alignment of the graphene gated to the CNP for the cases with and without strain. Different gate voltages are needed to gate the graphene to the CNP due to the strain-induced changes in the Dirac point energy (see Supplementary Note 1 for details). At the CNP, the strain-induced scalar potential at $\Delta z = 0.8$ mm can be directly extracted from Fig. 4 and the inset of Fig. 2b as:

$$S^{\Delta z=0.8 \text{ mm}} = -\Delta W_G^0 = -e\Delta V_{\text{CNP}} \approx -8 \text{ meV}. \quad (2)$$

To determine s_0 in Eq. (1), we need to estimate the applied strain. This we achieve using spatially resolved Raman spectroscopy at room temperature on the same device^{31,45–49}. For small uniaxial strain, a single Lorentzian describes the graphene Raman 2D peak, with the center frequency ω_{2D} redshifting linearly with increasing tensile strain. Figure 5 shows the mean center frequency $\bar{\omega}_{2D}$ averaged over the entire device area as a function of Δz . With increasing Δz , $\bar{\omega}_{2D}$ shifts to lower values, indicating an increasing average strain in the graphene³¹. Since the displacement Δz is much smaller than the length of the substrate, the strain increases linearly with Δz , with a slope of $\sim 14.3 \text{ cm}^{-1}$ per mm extracted by linear fitting. Using $\partial\omega_{2D}/\partial\varepsilon = -54 \text{ cm}^{-1}/\%$ from the literature⁴⁵, which is based on a theoretical calculation and agrees well with most of the reported experimentally extracted values for graphene on a substrate^{46–49}, we obtain a value for the induced tensile strain of $\varepsilon = \varepsilon_{xx} + \varepsilon_{yy} \approx 0.21\%$ at $\Delta z = 0.8$ mm. With this calibration of the strain value, we now deduce the characteristic scalar potential constant $s_0 = -S/\varepsilon \approx 3.8 \text{ eV}$, which is within the range predicted by theory^{6,8,9} and is consistent with the most recent calculations⁸.

As the last step, we exclude alternative explanations for the observed phenomenon. First, it is conceivable that bending the sample causes a redistribution of impurities (such as polymer residues). However, one can expect that such rearrangements would occur in a random manner and thus would not change the conductance features systematically with increasing strain, nor would the changes be reversible when decreasing the strain again. In contrast, our experiments exhibit clear, systematic, and monotonic shifts of the entire conductance curves with increasing strain and, most importantly, this effect is reversible for several increasing and decreasing straining cycles. In addition, we find the CNP shifts to the same direction with strain for a device with an opposite offset doping (see Supplementary Note 6), demonstrating that the effect is independent of the offset doping, which one would not expect for an impurity related mechanism. Second, the strain might affect the contact resistance, which adds in series to the total two-terminal device resistance. Therefore, a change in contact resistance would change the magnitude of the measured conductance values, but cannot lead to a constant shift of the conductance features, such as the CNP or the QHE plateaus, with respect to the gate voltage axis. Third, bending the substrate might induce changes in the gate capacitance, as found in suspended samples, resulting in a rescaling of the conductance curves with respect to zero gate voltage^{29,31}. This is clearly not the case in our experiments, because the gate capacitance is constant while straining due to the encapsulation and the support by the

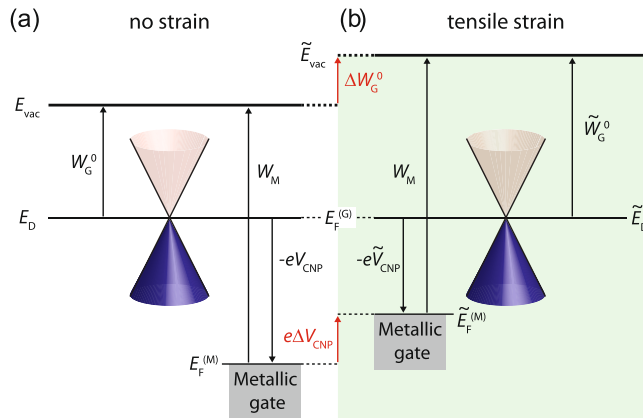


Fig. 4 Schematic energy level diagram. **a** Energy level diagram of the device at the charge neutrality point (CNP) for unstrained and **b** strained (green shaded) graphene. The Fermi levels of the graphene and the metallic gate are denoted $E_F^{(G)}$ and $E_F^{(M)}$ ($\tilde{E}_F^{(M)}$), respectively. The work function (WF) of the metallic gate is denoted W_M , assumed to be a constant. In our measurements, the graphene is grounded and therefore $E_F^{(G)}$ is fixed. The gate voltages tuning the graphene to the CNP for the unstrained and strained cases are denoted V_{CNP} and \tilde{V}_{CNP} , respectively. The WF difference of undoped graphene between with and without strain is denoted ΔW_G^0 .

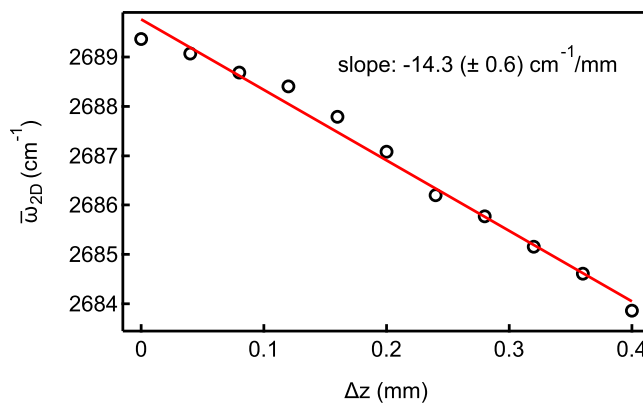


Fig. 5 Raman measurements for extracting the strain value. Spatially averaged center frequency $\bar{\omega}_{2D}$ of the Raman 2D peak plotted as a function of the displacement Δz . Black circles are data points. The error bars from the single Lorentzian fitting when extracting the center frequency of the Raman 2D peak are smaller than the data points. The red line is a linear fit to the data. The linear decrease with increasing Δz indicates an increasing average strain.

substrate³¹. Instead of rescaling, our experiments show a shift of the entire conductance curve with strain, consistent with a strain-induced scalar potential.

In conclusion, we have demonstrated how large-scale homogeneous strain in a graphene electronic device results in a scalar potential, which we detect using transport experiments in two different regimes. Combined with strain values extracted from Raman spectroscopy on the same device, we report the first systematically measured characteristic number for the scalar potential strength, consistent with the most recent theoretical calculations. This in situ strain tuning and the combination of transport and Raman measurements thus confirms the scalar potential as the origin of the observed strain effects. Our study forms the basis to investigate strain effects in transport experiments, which is crucial for future strain engineering in graphene and related 2D materials, such as generating a strain-induced in-plane electric field for observing the phenomenon of the Landau level collapse⁸, realizing

graphene quantum strain transistors⁵⁰, creating a pseudo-magnetic field with a non-uniform strain field^{9,11}, or realizing topological phases in van der Waals heterostructures^{51,52}.

Methods

Fabrication and Raman measurements. The hBN/graphene/hBN heterostructures were first assembled using the standard pick-up technique with a PDMS/PC stamp and then deposited onto the metallic gate structure prefabricated on a polyimide-coated phosphor bronze plate³¹. The typical thickness for the top (bottom) hBN is ~20 nm (~30 nm). The graphene flake was exfoliated from natural graphite. One-dimensional edge contacts⁵³ (Cr/Au, 5 nm/110 nm) were made to electrically connect the graphene. A controlled etching recipe was employed to stop in the middle of the bottom hBN and the remaining hBN acts as the insulating layer between the metallic leads and the bottom gate³¹.

The Raman measurements at room temperature were performed to determine the strain after the low-temperature transport measurements. A commercially available confocal Raman system WiTec alpha300 was used. The Raman spectra were acquired using a linearly polarized green laser (532 nm) with a power of 1.5 mW. The grating of the spectrometer is 600 grooves/mm.

Data availability

All data in this publication are available in numerical form at: <https://doi.org/10.5281/zenodo.4794596>.

Received: 17 January 2021; Accepted: 7 June 2021;

Published online: 29 June 2021

References

- Castro Neto, A. H., Guinea, F., Peres, N. M. R., Novoselov, K. S. & Geim, A. K. The electronic properties of graphene. *Rev. Mod. Phys.* **81**, 109–162 (2009).
- Das Sarma, S., Adam, S., Hwang, E. H. & Rossi, E. Electronic transport in two-dimensional graphene. *Rev. Mod. Phys.* **83**, 407–470 (2011).
- Goerbig, M. O. Electronic properties of graphene in a strong magnetic field. *Rev. Mod. Phys.* **83**, 1193–1243 (2011).
- Yankowitz, M., Ma, Q., Jarillo-Herrero, P. & LeRoy, B. J. van der waals heterostructures combining graphene and hexagonal boron nitride. *Nat. Rev. Phys.* **1**, 112–125 (2019).
- Pereira, V. M., Castro Neto, A. H. & Peres, N. M. R. Tight-binding approach to uniaxial strain in graphene. *Phys. Rev. B* **80**, 045401 (2009).
- Choi, S.-M., Jhi, S.-H. & Son, Y.-W. Effects of strain on electronic properties of graphene. *Phys. Rev. B* **81**, 081407(R) (2010).
- de Juan, F., Sturla, M. & Vozmediano, M. A. H. Space dependent fermi velocity in strained graphene. *Phys. Rev. Lett.* **108**, 227205 (2012).
- Grassano, D. et al. Work function, deformation potential, and collapse of landau levels in strained graphene and silicene. *Phys. Rev. B* **101**, 245115 (2020).
- Guinea, F., Geim, A. K., Katsnelson, M. I. & Novoselov, K. S. Generating quantizing pseudomagnetic fields by bending graphene ribbons. *Phys. Rev. B* **81**, 035408 (2010).
- Fogler, M. M., Guinea, F. & Katsnelson, M. I. Pseudomagnetic fields and ballistic transport in a suspended graphene sheet. *Phys. Rev. Lett.* **101**, 226804 (2008).
- Guinea, F., Katsnelson, M. I. & Geim, A. K. Energy gaps and a zero-field quantum hall effect in graphene by strain engineering. *Nat. Phys.* **6**, 30 (2009).
- Low, T. & Guinea, F. Strain-induced pseudomagnetic field for novel graphene electronics. *Nano Lett.* **10**, 3551–3554 (2010).
- Uchoa, B. & Barlas, Y. Superconducting states in pseudo-landau-levels of strained graphene. *Phys. Rev. Lett.* **111**, 046604 (2013).
- Zhu, S., Strosio, J. A. & Li, T. Programmable extreme pseudomagnetic fields in graphene by a uniaxial stretch. *Phys. Rev. Lett.* **115**, 245501 (2015).
- Levy, N. et al. Strain-induced pseudo-magnetic fields greater than 300 tesla in graphene nanobubbles. *Science* **329**, 544–547 (2010).
- Klimov, N. N. et al. Electromechanical properties of graphene drumheads. *Science* **336**, 1557–1561 (2012).
- Yan, H., Sun, Y., He, L., Nie, J.-C. & Chan, M. H. W. Observation of landau-level-like quantization at 77 k along a strained-induced graphene ridge. *Phys. Rev. B* **85**, 035422 (2012).
- Guo, D. et al. Observation of landau levels in potassium-intercalated graphite under a zero magnetic field. *Nat. Commun.* **3** (2012). <https://www.nature.com/articles/ncomms2072>.
- Lu, J., Neto, A. H. C. & Loh, K. P. Transforming moiré blisters into geometric graphene nano-bubbles. *Nat. Commun.* **3**, 823 (2012).
- Jiang, Y. et al. Visualizing strain-induced pseudomagnetic fields in graphene through an hbn magnifying glass. *Nano Lett.* **17**, 2839–2843 (2017).
- Liu, Y. et al. Tailoring sample-wide pseudo-magnetic fields on a graphene-black phosphorus heterostructure. *Nat. Nanotechnol.* **13**, 828–834 (2018).
- Jia, P. et al. Programmable graphene nanobubbles with three-fold symmetric pseudo-magnetic fields. *Nat. Commun.* **10**, 3127 (2019).
- Li, S.-Y., Su, Y., Ren, Y.-N. & He, L. Valley polarization and inversion in strained graphene via pseudo-landau levels, valley splitting of real landau levels, and confined states. *Phys. Rev. Lett.* **124**, 106802 (2020).
- He, X. et al. Tuning the graphene work function by uniaxial strain. *Appl. Phys. Lett.* **106**, 043106 (2015).
- Volodin, A., Van Haesendonck, C., Leenaerts, O., Partoens, B. & Peeters, F. M. Stress dependence of the suspended graphene work function: Vacuum kelvin probe force microscopy and density functional theory. *Appl. Phys. Lett.* **110**, 193101 (2017).
- Nigge, P. et al. Room temperature strain-induced landau levels in graphene on a wafer-scale platform. *Sci. Adv.* **5** (2019). <https://advances.sciencemag.org/content/5/11/eaaw5593>.
- Shioya, H., Russo, S., Yamamoto, M., Craciun, M. F. & Tarucha, S. Electron states of uniaxially strained graphene. *Nano Lett.* **15**, 7943–7948 (2015).
- Wu, Y. et al. Quantum wires and waveguides formed in graphene by strain. *Nano Lett.* **18**, 64–69 (2018).
- Huang, M., Pascal, T. A., Kim, H., Goddard, W. A. & Greer, J. R. Electronic-mechanical coupling in graphene from in situ nanoindentation experiments and multiscale atomistic simulations. *Nano Lett.* **11**, 1241–1246 (2011).
- Guan, F. & Du, X. Random gauge field scattering in monolayer graphene. *Nano Lett.* **17**, 7009–7014 (2017).
- Wang, L. et al. In situ strain tuning in hBN-encapsulated graphene electronic devices. *Nano Lett.* **19**, 4097–4102 (2019).
- Cahen, D. & Kahn, A. Electron energetics at surfaces and interfaces: concepts and experiments. *Adv. Mater.* **15**, 271–277 (2003).
- Wang, L. et al. Mobility enhancement in graphene by in situ reduction of random strain fluctuations. *Phys. Rev. Lett.* **124**, 157701 (2020).
- Du, R. et al. Tuning anti-klein to klein tunneling in bilayer graphene. *Phys. Rev. Lett.* **121**, 127706 (2018).
- Wang, L. et al. New generation of moiré superlattices in doubly aligned hbn/graphene/hbn heterostructures. *Nano Lett.* **19**, 2371–2376 (2019).
- Young, A. F. & Kim, P. Quantum interference and klein tunnelling in graphene heterojunctions. *Nat. Phys.* **5**, 222 (2009).
- Rickhaus, P. et al. Ballistic interferences in suspended graphene. *Nat. Commun.* **4** (2013). <https://doi.org/10.1038/ncomms3342>.
- Grushina, A. L., Ki, D.-K. & Morpurgo, A. F. A ballistic pn junction in suspended graphene with split bottom gates. *Appl. Phys. Lett.* **102**, 223102 (2013).
- Handschin, C. et al. Fabry-pérot resonances in a graphene/hbn moiré superlattice. *Nano Lett.* **17**, 328–333 (2017).
- Bolotin, K. I., Ghahari, F., Shulman, M. D., Stormer, H. L. & Kim, P. Observation of the fractional quantum hall effect in graphene. *Nature* **462**, 196–199 (2009).
- Du, X., Skachko, I., Duerr, F., Luican, A. & Andrei, E. Y. Fractional quantum hall effect and insulating phase of dirac electrons in graphene. *Nature* **462**, 192–195 (2009).
- Dean, C. R. et al. Multicomponent fractional quantum hall effect in graphene. *Nat. Phys.* **7**, 693–696 (2011).
- Özyilmaz, B. et al. Electronic transport and quantum hall effect in bipolar graphene $p-n-p$ junctions. *Phys. Rev. Lett.* **99**, 166804 (2007).
- Amet, F., Williams, J. R., Watanabe, K., Taniguchi, T. & Goldhaber-Gordon, D. Selective equilibration of spin-polarized quantum hall edge states in graphene. *Phys. Rev. Lett.* **112**, 196601 (2014).
- Mohr, M., Papagelis, K., Maultzsch, J. & Thomsen, C. Two-dimensional electronic and vibrational band structure of uniaxially strained graphene from ab initio calculations. *Phys. Rev. B* **80**, 205410 (2009).
- Mohiuddin, T. M. G. et al. Uniaxial strain in graphene by raman spectroscopy: g peak splitting, gröneisen parameters, and sample orientation. *Phys. Rev. B* **79**, 205433 (2009).
- Huang, M., Yan, H., Heinz, T. F. & Hone, J. Probing strain-induced electronic structure change in graphene by raman spectroscopy. *Nano Lett.* **10**, 4074–4079 (2010).
- Yoon, D., Son, Y.-W. & Cheong, H. Strain-dependent splitting of the double-resonance raman scattering band in graphene. *Phys. Rev. Lett.* **106**, 155502 (2011).
- Frank, O. et al. Raman 2d-band splitting in graphene: Theory and experiment. *ACS Nano* **5**, 2231–2239 (2011).
- McRae, A. C., Wei, G. & Champagne, A. R. Graphene quantum strain transistors. *Phys. Rev. Appl.* **11**, 054019 (2019).
- Tajkov, Z., Visontai, D., Oroszlány, L. & Koltai, J. Uniaxial strain induced topological phase transition in bismuth-tellurohalide-graphene heterostructures. *Nanoscale* **11**, 12704–12711 (2019).
- Tajkov, Z., Koltai, J., Cserti, J. & Oroszlány, L. Competition of topological and topologically trivial phases in patterned graphene based heterostructures. *Phys. Rev. B* **101**, 235146 (2020).

53. Wang, L. et al. One-dimensional electrical contact to a two-dimensional material. *Science* **342**, 614–617 (2013).

Acknowledgements

This work has received funding from the Swiss Nanoscience Institute (SNI), the ERC project TopSupra (787414), the European Union Horizon 2020 research and innovation programme under grant agreement No. 785219 (Graphene Flagship), the Swiss National Science Foundation, the Swiss NCCR QSIT and from the OTKA FK-123894 grants. P.M. acknowledges support from the Bolyai Fellowship, the Marie Curie grant, Topograph Flagera network and the National Research, Development, and Innovation Fund of Hungary within the Quantum Technology National Excellence Program (Project No. 2017-1.2.1-NKP-2017-00001). K.W. and T.T. acknowledge support from the Elemental Strategy Initiative conducted by the MEXT, Japan, Grant Number JPMXP012101001, JSPS KAKENHI Grant Numbers JP20H00354 and the CREST(JPMJCR15F3), JST. We thank Francisco Guinea, Peter Rickhaus, János Koltai, László Oroszlány, Zoltán Tajkov and András Pályi for fruitful discussions, and Sascha Martin and his team for their technical support.

Author contributions

L.W. fabricated the devices, performed the measurements, and did the data analysis. A.B., P.M., S.Z., and C.S. helped to understand the data. B.V. performed parts of the Raman measurements. D.I. supported the sample fabrication. K.W. and T.T. provided the high-quality hBN. C.S. initiated and supervised the project. L.W. and A.B. wrote the paper and all authors discussed the results and worked on the manuscript.

Competing interests

The authors declare no competing interests.

Additional information

Supplementary information The online version contains supplementary material available at <https://doi.org/10.1038/s42005-021-00651-y>.

Correspondence and requests for materials should be addressed to L.W.

Peer review information *Communications Physics* thanks the anonymous reviewers for their contribution to the peer review of this work. Peer reviewer reports are available.

Reprints and permission information is available at <http://www.nature.com/reprints>

Publisher's note Springer Nature remains neutral with regard to jurisdictional claims in published maps and institutional affiliations.



Open Access This article is licensed under a Creative Commons Attribution 4.0 International License, which permits use, sharing, adaptation, distribution and reproduction in any medium or format, as long as you give appropriate credit to the original author(s) and the source, provide a link to the Creative Commons license, and indicate if changes were made. The images or other third party material in this article are included in the article's Creative Commons license, unless indicated otherwise in a credit line to the material. If material is not included in the article's Creative Commons license and your intended use is not permitted by statutory regulation or exceeds the permitted use, you will need to obtain permission directly from the copyright holder. To view a copy of this license, visit <http://creativecommons.org/licenses/by/4.0/>.

© The Author(s) 2021